

# NEOWISE Observations Of The Potentially Hazardous Asteroid (99942) Apophis

AKASH SATPATHY <sup>1</sup>, AMY MAINZER <sup>1</sup>, JOSEPH R. MASIERO <sup>2</sup>, TYLER LINDER <sup>3</sup>,  
ROC M. CUTRI <sup>2</sup>, EDWARD L. WRIGHT <sup>4</sup>, JANA PITTICHOVÁ,<sup>5</sup> TOMMY GRAV,<sup>1</sup> AND  
EMILY KRAMER <sup>5</sup>

<sup>1</sup>*Lunar and Planetary Laboratory, University of Arizona, Tucson, AZ, USA*

<sup>2</sup>*Caltech-IPAC, Pasadena, CA, USA*

<sup>3</sup>*Astronomical Research Institute, Ashmore, IL, USA*

<sup>4</sup>*UCLA Astronomy, Los Angeles, CA, USA*

<sup>5</sup>*Jet Propulsion Laboratory, California Institute of Technology, Pasadena, CA, USA*

## ABSTRACT

Large potentially hazardous asteroids (PHAs) are capable of causing a global catastrophe in the event of a planetary collision. Thus, rapid assessment of such an object’s physical characteristics is crucial for determining its potential risk scale. We treated the near-Earth asteroid (99942) Apophis as a newly discovered object during its 2020-2021 close-approach as part of a mock planetary defense exercise. The object was detected by the Near-Earth Object Wide-field Infrared Survey Explorer (NEOWISE), and data collected by the two active bands (3.4  $\mu\text{m}$  and 4.6  $\mu\text{m}$ ) were analyzed using thermal and thermophysical modeling. Our results indicate that Apophis is an elongated object with an effective spherical diameter  $D_{\text{eff}} = 340 \pm 70$  m, a geometric visual albedo  $p_V = 0.31 \pm 0.09$ , and a thermal inertia  $\Gamma \sim 150 - 2850 \text{ Jm}^{-2}\text{s}^{-\frac{1}{2}}\text{K}^{-1}$  with a best-fit value of  $550 \text{ Jm}^{-2}\text{s}^{-\frac{1}{2}}\text{K}^{-1}$ . NEOWISE “discovery” observations reveal that (99942) Apophis is a potentially hazardous asteroid that would likely cause damage at a regional level and not a global one.

*Keywords:* Near-Earth objects(1092) — Close encounters(255) — Infrared Astronomical Satellite(785) — Photometry(1234) — Computational astronomy(293) — Markov chain Monte Carlo(1889) — Astronomy data modeling(1859)

## 1. OVERVIEW

Near-Earth Asteroids (NEAs) are a sub-population of asteroids that pass very close to the Earth. They are conventionally defined as small bodies with a perihelion distance

less than or equal to 1.3 au, and compared to Main-Belt Asteroids (MBAs), they tend to be smaller in size and irregularly shaped with short dynamical lifespans. Due to their relative proximity to the Earth, detailed studies of their physical characteristics such as diameter, albedo, thermal inertia, rotational period, and absolute visual magnitude can be performed by

using data obtained from either remote sensing (Ostro 1993, Werner et al. 2004, and Mainzer et al. 2011a) or in-situ (Watanabe et al. 2017, Lauretta et al. 2017) missions. Studying these features can help us theorize their origin and evolution in the solar system (as laid out by Binzel et al. 1992, Michel et al. 2005, Granvik & Brown 2018, and others), and take pivotal steps towards planetary defense.

NEAs with a Minimum Orbit Intersection Distance (MOID) to the Earth of less than 0.05 au and an H magnitude less than or equal to 22 (or correspondingly, a minimum diameter of roughly 140 meters) are formally classified as Potentially Hazardous Asteroids or PHAs as they have the capability to cause substantial damage upon collision with the Earth. One example from recorded history is the 1908 Tunguska event, where a meteor with a diameter of  $\sim 100$  meters exploded over a Siberian forest, producing around 60 PJ of energy and affecting an area as large as 2150 km<sup>2</sup> (Vasilyev 1998). A more recent and better-documented example is the 2013 Chelyabinsk event where a small NEA about 19 meters in diameter (Borovička et al. 2013) exploded over Chelyabinsk Oblast, Russia, injuring roughly 1500 people and damaging around 7200 buildings. Therefore, the discovery and categorization of such asteroids are crucial to prevent potential impacts and mitigate harm.

A particular NEA — (99942) Apophis — has been an object of great interest since its discovery in 2004 by R. A. Tucker, D. J. Tholen, and F. Bernardi. It is a well-known PHA with a catalog H magnitude of 19.7, a perihelion distance of roughly 0.746 au, and a MOID of 0.0002056 au. Thousands of optical and dozens of radar observations have allowed planetary scientists to study Apophis in great detail. Binzel et al. (2009) studied its spectral properties and composition and categorized it as an Sq-class

asteroid (Bus 1999 and DeMeo et al. 2009), and Lin et al. (2018) classified it as an S-class asteroid (Tholen 1984) after carrying out a photometric survey. Delbo et al. (2007) used polarimetric observations to estimate its size and albedo, and Müeller et al. (2014) used thermal measurements from Herschel to determine its size, albedo, thermal inertia, and also calculated its mass by using Itokawa’s density and porosity. The most recent results based on radar observations from Goldstone and Arecibo suggest that Apophis is an elongated, asymmetric, and possibly bifurcated object with a diameter of  $340 \pm 40$  m and a visible geometric albedo of  $0.35 \pm 0.10$  (Brozović et al. 2018).

Post-discovery, Apophis drew international attention when its collision probability was initially estimated to be as high as 2.7% for the year 2029. It was speculated that it might enter a so-called gravitational keyhole, which could exacerbate the possibility of an impact in the year 2036. Follow-up studies and analysis significantly lowered this probability, and any chance of collision in 2029 and 2036 was ruled out. Recent radar observations from Goldstone also eliminated the slight risk of impact for the year 2068 and further showed that it posed no threat to the Earth for at least another hundred years.<sup>1</sup> Nonetheless, Apophis remained a “virtual impactor” of special interest to the planetary defense community and was the subject of a mock planetary defense exercise during its 2020-2021 flyby.

In the exercise, Apophis was treated as a newly discovered asteroid, and the capability of research groups to identify and rapidly characterize potentially hazardous objects were tested (inspired by a similar activity performed by

<sup>1</sup> <https://echo.jpl.nasa.gov/asteroids/Apophis/apophis.2021.goldstone.planning.html>

Reddy et al. 2019 where they tracked and characterized the NEA 2012 TC4 as a hypothetical impactor). Thermal infrared data on (99942) Apophis was collected by the Near-Earth Object Wide-field Infrared Survey Explorer (NEOWISE; Mainzer et al. 2014, Wright et al. 2010) during the object’s close approaches in December of 2020 and March-April of 2021. These new observations resulted in the “discovery” of the object, and its diameter and albedo were rapidly computed following standard image processing and calibration by the NEOWISE data system (Cutri et al. 2015). While a forthcoming publication will describe the full results of the mock exercise, our study reconfirms prior results and highlights the accuracy and speed of the NEOWISE team’s analytical methods.

## 2. OBSERVATIONS

The Near-Earth Object Wide-field Infrared Survey Explorer (NEOWISE; Mainzer et al. 2014) is a two-band all-sky thermal infrared survey well suited to investigating the physical properties of asteroids and comets. It was initially launched as the Wide-field Infrared Survey Explorer (WISE; Wright et al. 2010) in December of 2009 with the objective to map 99% of the sky using four thermal IR bands with wavelengths 3.4, 4.6, 12, and 22  $\mu\text{m}$  (named W1, W2, W3, and W4, respectively). The primary mission concluded after the solid hydrogen coolant was exhausted and the W3 and W4 channels ceased to function, and WISE was put into hibernation in February 2011. In December 2013, the spacecraft was reactivated and repurposed as NEOWISE with the W1 and W2 channels active, and since that time has detected over 40,000 different solar system small

bodies.<sup>2</sup>

NEOWISE was one of the first surveys to submit “discovery” tracklets (sets of position-time measurements of candidate moving objects) for Apophis late in 2020. Thirty-one single exposure detections were acquired during the two observing epochs (see figure 1 for reference). First, the detections were automatically ingested by the WISE Moving Object Pipeline Subsystem (WMOPS) that associates sets of detections with apparent on-sky motions that are consistent with orbital motion. Detections were rejected if they had moon separation angles (*moon\_sep*) of less than  $15^\circ$ , were saturated,<sup>3</sup> were co-located within 6.5 arcsec of stationary, background objects such as stars or galaxies (identified from the AllWISE Atlas Image set from Cutri et al. 2013), or had poor fits to the reference point spread functions i.e. a *w1rchi2*  $\geq 5$  and *w2rchi2*  $\geq 5$  (most likely due to cosmic rays).<sup>4</sup> Lastly, the detection images were visually inspected to check for any other unflagged artifacts, and additional scan frames were extracted using the WISE Moving Object Search Tool (MOST) as a few detections were rejected by WMOPS due to the curvature of their on-sky motion or falling near a background object.<sup>5</sup>

From the first epoch in December 2020, seventeen detections were identified in the two active bands (3.4  $\mu\text{m}$  and 4.6  $\mu\text{m}$ ), with an observation time spanning 32.75 hours. The SNR at 4.6  $\mu\text{m}$  was approximately 5.5, and the solar elongation angle was roughly  $90^\circ$ . Eight additional detections were collected during the second observing epoch in April 2021, spanning 17.25 hours with

<sup>2</sup> <https://wise2.ipac.caltech.edu/docs/release/neowise/>

<sup>3</sup> [https://wise2.ipac.caltech.edu/docs/release/neowise/expsup/sec2\\_1civa.html](https://wise2.ipac.caltech.edu/docs/release/neowise/expsup/sec2_1civa.html)

<sup>4</sup> [https://wise2.ipac.caltech.edu/docs/release/neowise/expsup/sec2\\_1a.html](https://wise2.ipac.caltech.edu/docs/release/neowise/expsup/sec2_1a.html)

<sup>5</sup> <https://irsa.ipac.caltech.edu/applications/MOST/>

**Table 1.** Observing geometry of (99942) Apophis during the two NEOWISE observing epochs.

Epoch	MJD	WISE-centric distance au	Heliocentric distance au	Solar Elongation Degrees	Phase Angle Degrees
1	59202.561219	0.259	1.018	90.2	75.1
2	59305.273533	0.137	1.057	111.2	61.8

NOTE—For Epoch 1, the start and end date and time were 18-12-2020 at 23:26:13 and 20-12-2020 at 08:23:39, respectively. For Epoch 2, the start and end date and time were 31-03-2021 at 21:49:28 and 01-04-2021 at 15:04:56, respectively.

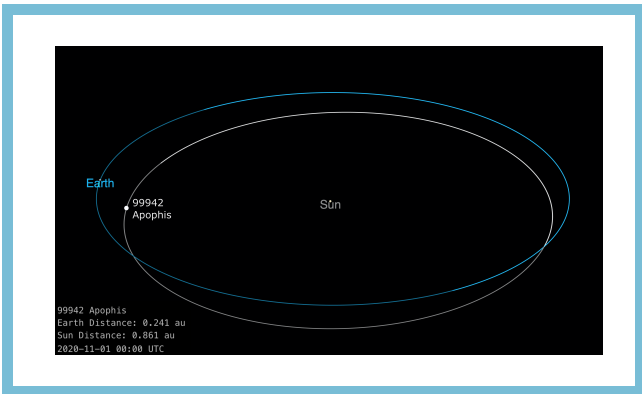


**Figure 1.** A seventeen second long video that shows (99942) Apophis and the Earth’s motion from November 2020 to May 2021. The animation is available in the HTML version of this article. The first and second epoch of observations are labelled with the help of freeze frames. The name of object, the distance to Earth and the Sun, and the date and time are notated at the bottom-left corner. The video was made with the help of the [JPL Small-Body Database Browser](#).

an average SNR of 32.7 at 4.6  $\mu\text{m}$  and a solar elongation angle of about  $110^\circ$ . The SNR was noticeably higher during the second epoch because Apophis was closer to the Earth than it was during the first epoch. A summary of the observing geometry can be found in Table 1, and detailed information about the same is given in Table 3.

Lastly, visible photometry nearly simultaneous to Epoch 1 was obtained using the SMARTS 1.0-meter telescope from the Cerro Tololo Inter-

American Observatory (CTIO) was used to provide an improved constraint on the absolute visual magnitude i.e.  $H$  (as  $H$  magnitudes for many asteroids, particularly near-Earth objects, often have large uncertainties, which in turn reduces the accuracy of derived visible albedos). SMARTS 1.0 meter is a Boller and Chivens  $f/10.5$  telescope with a back-illuminated Finger Lakes Instruments thermo-electrically cooled camera that has 13.5  $\mu\text{m}$  pixels and an array size of 2048 x 2048 pixels. Data were taken continuously on the 18th of December, 2020 from 06:54 to 08:18 UTC with filters in the following order: Clear,  $g$ ,  $r$ ,  $i$ ,  $z$ , B, and, V. There was a  $\sim 3$  second delay between exposures while the filter wheel moved. In total, 112 images were taken, i.e., 16 exposures for each of the seven filters. The pixel binning size was set to 4, which produced a 1.05 arcsec per pixel image scale. The data were calibrated to Pan-STARRS, and Kostov & Bonev (2018) were referenced to convert Pan-STARRS  $g$ ,  $r$ ,  $i$  values to B and V (see Table 2 in that paper). These transformed V values, listed in Table 2 and plotted in Figure 2, were then used to calibrate the V filter and compute an  $H = 19.1 \pm 0.5$  using the  $HG$ -system delineated in [Bowell et al. 1989](#) ( $G = 0.25 \pm 0.20$  from [Shevchenko et al. 2019](#) was assumed during the conversion).

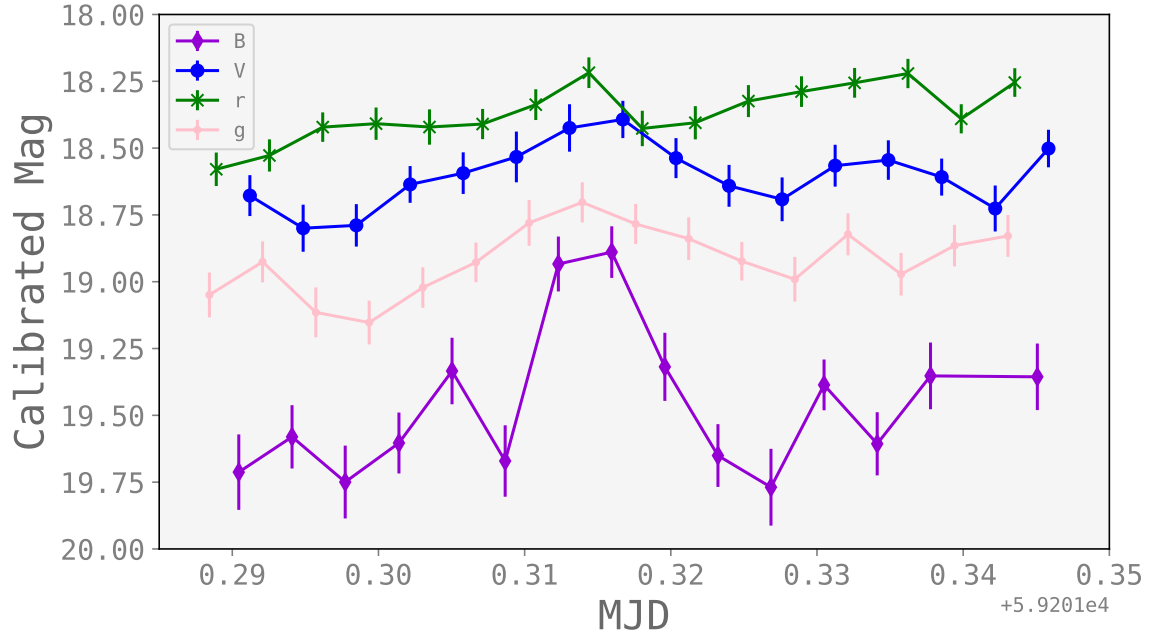


**Figure 2.** CTIO observations in B, V,  $r$ , and  $g$ ; taken at nearly the same time as NEOWISE’s first epoch of observations.

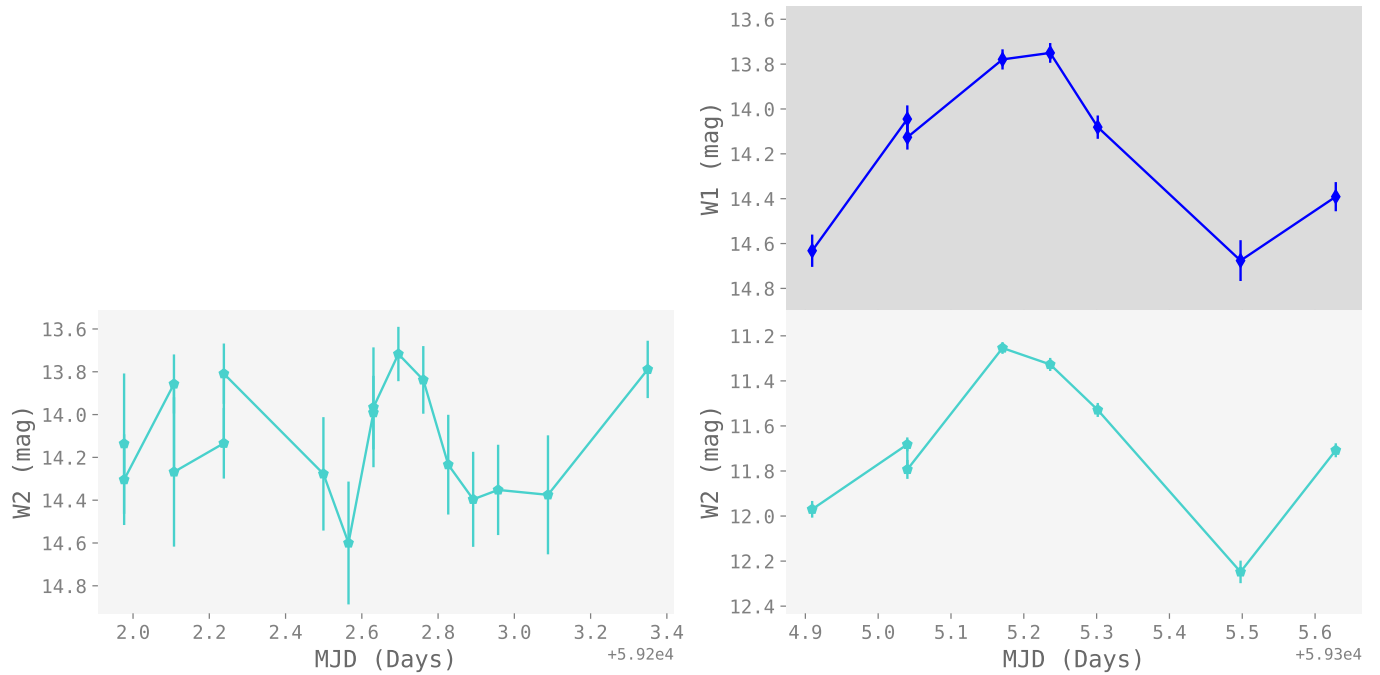


**Figure 3.** Lightcurves from the first and second observing epochs (left and right, respectively). The W1 band data from the first epoch was omitted due to marginal detections. The large amplitude in the lightcurves suggest that the object has an elongated shape, as previously shown by Brozović et al. (2018).

**Table 2.** Truncated table of CTIO observations of (99942) Apophis in B, *g*, *r*, and V.

Filter	MJD	RA	Dec	Zero Point	Instantaneous Mag	Calibrated Mag
		Degrees	Degrees	Mag	Mag	Mag
<b>B</b>	59201.290444	172.42233	-10.59855	27.342 ± 0.048	-7.630 ± 0.133	19.713 ± 0.141
	59201.294088	172.42300	-10.59945	27.575 ± 0.057	-7.995 ± 0.104	19.581 ± 0.118
	59201.297726	172.42366	-10.60035	27.382 ± 0.061	-7.632 ± 0.122	19.750 ± 0.136
				...		
<b>V</b>	59201.291203	172.42246	-10.59873	26.997 ± 0.038	-8.319 ± 0.066	18.678 ± 0.077
	59201.294848	172.42313	-10.59963	27.010 ± 0.053	-8.210 ± 0.070	18.800 ± 0.088
	59201.298486	172.42379	-10.60053	27.012 ± 0.049	-8.223 ± 0.062	18.789 ± 0.079
	59201.302166	172.42459	-10.60161	27.022 ± 0.037	-8.386 ± 0.058	18.636 ± 0.069
	59201.305797	172.42525	-10.60251	27.029 ± 0.044	-8.435 ± 0.065	18.594 ± 0.078
	59201.309434	172.42590	-10.60341	27.050 ± 0.053	-8.517 ± 0.079	18.533 ± 0.095
	59201.313071	172.42655	-10.60431	27.041 ± 0.060	-8.616 ± 0.065	18.425 ± 0.089
	59201.316718	172.42733	-10.60539	27.058 ± 0.036	-8.665 ± 0.059	18.393 ± 0.070
	59201.320353	172.42798	-10.60629	27.057 ± 0.036	-8.520 ± 0.066	18.538 ± 0.075
	59201.323983	172.42862	-10.60719	27.075 ± 0.055	-8.434 ± 0.056	18.641 ± 0.078
	59201.327613	172.42927	-10.60809	27.071 ± 0.050	-8.379 ± 0.065	18.692 ± 0.082
	59201.331241	172.42990	-10.60899	27.045 ± 0.057	-8.479 ± 0.054	18.566 ± 0.078
	59201.334881	172.43067	-10.61006	27.029 ± 0.047	-8.484 ± 0.057	18.545 ± 0.074
	59201.338529	172.43130	-10.61096	27.056 ± 0.044	-8.447 ± 0.053	18.608 ± 0.069
	59201.342191	172.43193	-10.61185	27.022 ± 0.053	-8.296 ± 0.068	18.726 ± 0.086
59201.345835	172.43269	-10.61293	27.045 ± 0.047	-8.543 ± 0.052	18.502 ± 0.070	

NOTE—The CTIO V-filter observations began on 18-12-2020 at 06:59:20 and ended on 18-12-2020 at 08:18:00 (i.e., separated from NEOWISE’s first epoch of observations by roughly 15 hours). The airmass during the first image was 1.6, and the same during last image was 1.22. Airmass was reducing during the observing run. All observations were taken during night-time and were four days past new moon (i.e., there was no moon effect). The table has been truncated for conciseness. All the values below the ellipses are in V, and observations in B, *g*, and *r* filters can be accessed in an electronic format. Only the median V-magnitude ( $18.60 \pm 0.11$ ) was used in this paper to constrain the H-mag.

**Table 3.** Two-epoch observations of (99942) Apophis in the 3.4  $\mu\text{m}$  and 4.6  $\mu\text{m}$  bands.

RA	Dec	MJD	Source ID	W1					W2				
				Mag	Mag $\sigma$	Flux	Flux $\sigma$	$\chi^2$	Mag	Mag $\sigma$	Flux	Flux $\sigma$	$\chi^2$
(1)	(2)	(3)	(4)	(5)	(6)	(7)	(8)	(9)	(10)	(11)	(12)	(13)	(14)
172.5647	-10.7728	59201.97654340	23614r158-002887	16.468	0.363	52.140	17.452	0.97	14.136	0.328	159.64	48.162	0.83
172.5647	-10.7723	59201.97667076	23614r159-002689	15.366	–	66.212	38.803	0.68	14.304	0.212	136.71	26.672	1.10
172.5938	-10.8056	59202.10731955	23618r158-001173	16.670	0.459	43.306	18.320	0.96	13.857	0.138	206.38	26.256	0.38
172.5941	-10.8058	59202.10744691	23618r159-000844	15.352	0.219	145.68	29.341	0.50	14.268	0.349	141.34	45.426	1.53
172.6229	-10.8388	59202.23809564	23622r158-002053	16.696	0.433	42.256	16.837	1.22	14.134	0.165	159.85	24.265	0.61
172.6232	-10.8387	59202.23822300	23622r159-001278	16.467	0.357	52.169	17.172	0.69	13.809	0.141	215.73	27.933	0.54
172.6808	-10.9049	59202.49926582	23630r146-010408	16.466	0.323	52.211	15.513	2.03	14.277	0.265	140.11	34.187	0.36
172.6957	-10.9209	59202.56509962	23632r134-001369	15.745	0.225	101.48	21.036	0.82	14.600	0.287	104.13	27.559	0.42
172.7095	-10.9375	59202.63042400	23634r158-000846	15.568	0.194	119.47	21.293	1.19	13.991	0.172	182.41	28.970	0.51
172.7097	-10.9370	59202.63055132	23634r159-001077	15.691	0.169	106.61	16.560	1.27	13.966	0.280	186.62	48.126	0.76
172.7240	-10.9540	59202.69587575	23636r134-001054	16.046	0.232	76.939	16.424	1.07	13.717	0.127	234.82	27.524	1.20
172.7384	-10.9703	59202.76120009	23638r158-001182	15.760	0.205	100.07	18.877	0.91	13.838	0.158	210.04	30.474	0.57
172.7531	-10.9868	59202.82665184	23640r134-002266	16.276	–	30.427	15.892	0.74	14.234	0.233	145.77	31.301	0.76
172.7674	-11.0035	59202.89197627	23642r158-002419	16.243	0.281	64.152	16.604	0.70	14.396	0.222	125.57	25.675	0.89
172.7817	-11.0200	59202.95742860	23644r134-002255	16.518	0.539	49.773	24.690	0.80	14.352	0.211	130.83	25.422	0.29
172.8100	-11.0526	59203.08820473	23648r134-002554	16.412	0.360	54.910	18.223	0.44	14.375	0.278	128.04	32.788	0.93
172.8671	-11.1186	59203.34975691	23656r134-001623	16.405	0.443	55.270	22.528	1.37	13.789	0.134	219.73	27.045	0.93
123.3184	10.9412	59304.90934705	26763r125-000449	14.632	0.072	282.76	18.878	0.80	11.970	0.037	1173.1	40.288	0.69
123.2764	11.0123	59305.03999583	26767r125-000363	14.045	0.061	485.89	27.342	1.04	11.682	0.031	1530.2	43.602	1.38
123.2764	11.0122	59305.04012315	26767r126-000374	14.126	0.055	450.68	22.704	1.36	11.793	0.042	1381.2	53.025	1.20
123.2347	11.0830	59305.17077185	26771r125-000262	13.779	0.045	620.66	25.547	0.99	11.254	0.026	2269.6	53.736	0.37
123.2140	11.1182	59305.23622361	26773r102-000306	13.750	0.044	637.32	26.031	3.08	11.327	0.029	2120.6	56.527	1.21
123.1934	11.1535	59305.30154795	26775r125-000328	14.081	0.052	469.71	22.316	1.45	11.529	0.031	1760.5	50.329	0.56
123.1322	11.2589	59305.49764841	26781r046-000549	14.676	0.091	271.52	22.695	1.30	12.248	0.050	907.84	42.166	0.71
123.0919	11.3287	59305.62842442	26785r102-000420	14.391	0.065	353.12	21.001	0.91	11.708	0.031	1493.9	42.510	0.82

NOTE—The horizontal line near the middle row separates the first and the second set of observations. The units for Ra and Dec are degrees, and that of flux is  $\mu\text{Jy}$ . Source ID in column (4) is a unique ID comprising of the scan ID, frame number, and source number. “Mag” in columns (5), (6), (10), and (11) refers to the instrumental profile-fit photometry magnitude of the object at the time of the observation. “ $\sigma$ ” in columns (6), (8), (11), and (13) represents the measurement uncertainty. The detailed methodology for the determination of in-band uncertainties and flux calibration uncertainties can be found in Cutri et al. (2015) Columns (9) and (14) contain the  $\chi^2$  statistic that show the [quality of the profile-fit photometry](#) of the measurements.

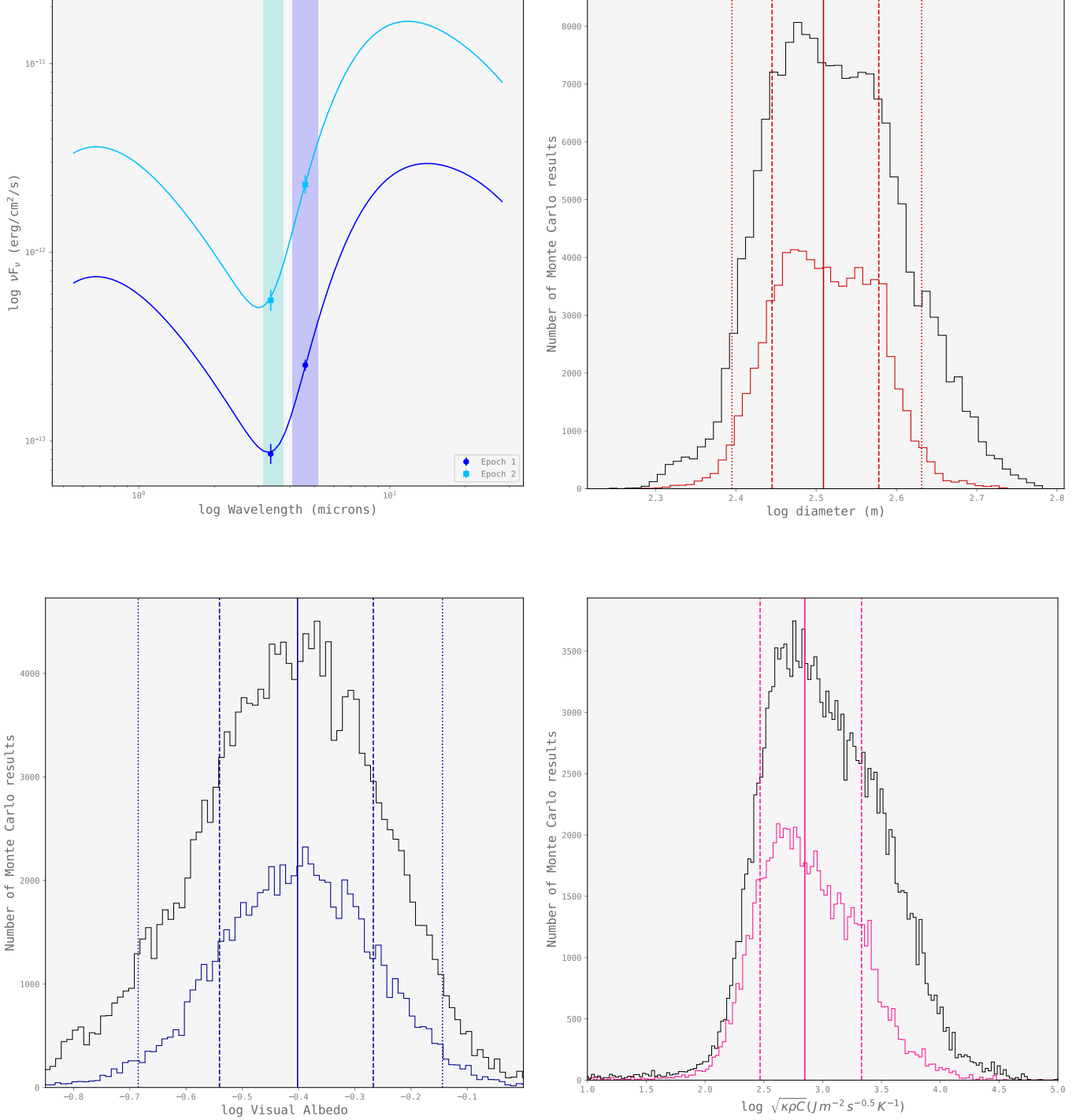


**Figure 4.** Plots highlighting the TPM results with (99942) Apophis modeled as a sphere. In a clockwise manner from the top-left: average flux density during the two epochs along with the span of the bandpasses (the average flux was  $95.77 \mu\text{Jy}$  in W1 and  $381.13 \mu\text{Jy}$  in W2 during the first epoch, and  $622.88 \mu\text{Jy}$  in W1 and  $3475.26 \mu\text{Jy}$  in W2 during the second epoch), histogram of the diameter results with the 68% (dashed lines) and 95% (dotted lines) confidence interval ranges, histogram of the thermal inertia results with the 68% (dashed lines) confidence interval range (the 95% confidence interval values lie outside the x-axis range), and histogram of the visual albedo results with the 68% (dashed lines) and 95% (dotted lines) confidence interval ranges. The fainter histograms in the top-right, bottom-left, and bottom-right plots signify the solutions without the LCDB pole solution constraint.



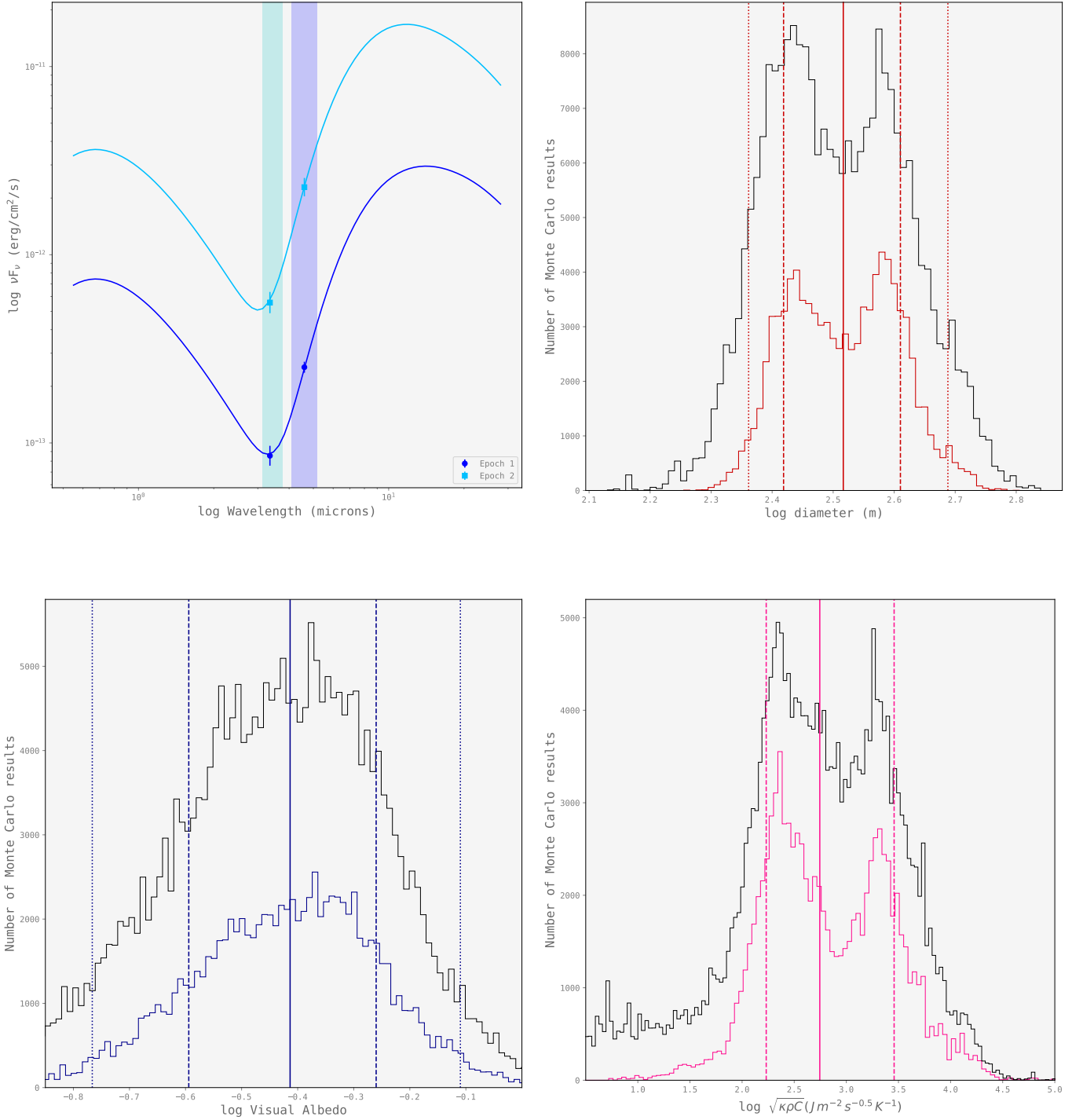


**Figure 5.** Plots highlighting the TPM results with (99942) Apophis modeled as a triaxial ellipsoid. In a clockwise manner from the top-left: average flux density during the two epochs along with the span of the bandpasses (the average flux was  $95.37 \mu\text{Jy}$  in W1 and  $385.73 \mu\text{Jy}$  in W2 during the first epoch, and  $621.31 \mu\text{Jy}$  in W1 and  $3496.75 \mu\text{Jy}$  in W2 during the second epoch), histogram of the diameter results with the 68% (dashed lines) and 95% (dotted lines) confidence interval ranges, histogram of the thermal inertia results with the 68% (dashed lines) confidence interval range (the 95% confidence interval values lie outside the x-axis range), and histogram of the visual albedo results with the 68% (dashed lines) and 95% (dotted lines) confidence interval ranges. The fainter histograms in the top-right, bottom-left, and bottom-right plots show the distribution without the LCDB pole solution constraint.

### 3. THERMAL MODELS AND RESULTS

Categorizing asteroids based on diameter and albedo by modeling their thermal emission (dominant in wavelengths greater than  $4\ \mu\text{m}$  for most near-Earth objects and asteroids closer than  $\sim 4$  au heliocentric distance) has become standard practice since infrared observations of small bodies began in the 1970s. Standard thermal models idealize asteroids as non-rotating spheres with a zero-degree solar phase angle. The asteroid model is bisected into a day and a night side, and it is assumed that the thermal emission on the dayside decreases from the subsolar point to the terminator, and that the night side has zero thermal emission. Following the temperature distribution, the reflected and absorbed sunlight on the dayside of the simplified asteroid model can be considered to be in equilibrium and can be used to compute the effective spherical diameter and bolometric Bond albedo. Next, the V-band geometric albedo can be determined using the system laid out by [Bowell et al. \(1989\)](#), which uses the absolute magnitude ( $H$ ) and phase slope coefficient ( $G$ ) to describe the phase curve function. Additional parameters, including the so-called beaming parameter, can be used to better constrain the results by correcting for variation in thermal emission due to surface and shape irregularities, thermal inertia and rotation, spectral slope, and differing observing geometries (see [Matson 1972](#), [Morrison 1973](#), [Jones & Morrison 1974](#), [Morrison & Chapman 1976](#), [Morrison & Lebofsky 1979](#), [Lebofsky & Spencer 1989](#), and [Harris & Lagerros 2002](#) for an extended discussion on the topic).

[Lebofsky et al. \(1986\)](#) computed an improved estimate of the beaming parameter based on observations of 1 Ceres and 2 Pallas and put forward the refined Standard Thermal Model (STM). While this model was demonstrated

to effectively determine the size and visual albedo of several MBAs, the same estimations for NEAs had significant deviations when compared to radiometric predictions ([Veeder et al. 1989](#)). Unlike the two very large main-belt objects that were used to calibrate the parameters of the refined STM, a typical NEA is observed at higher phase angles and has distinct physical and thermal properties. These confounding factors likely decreased the fidelity of the refined STM fits for the NEAs.

[Harris \(1998\)](#) developed a modified version of the refined STM called the Near-Earth Asteroid Thermal Model (NEATM) and presented revised diameter and visual albedo estimates with substantially better matches to independently measured diameters for several NEAs. Two primary improvements were implemented by [Harris](#): first, incorporating observing geometry in the calculations to account for flux variations that arise on the nightside and the dayside; and second, including a varying beaming parameter to figure in the assumption that the nightside had zero emission and for other uncertainties due to shape, spin pole, rotation rate, surface roughness, and thermal conductivity. The NEATM is capable of fitting the diameter, beaming, visible geometric albedo, and under certain circumstances, the albedo at shorter infrared wavelengths ( $3 - 4\ \mu\text{m}$ ). The precise number of parameters that can be fit depends on the number of measurements available. For asteroids detected by the reactivated NEOWISE mission, the brightnesses at  $3.4\ \mu\text{m}$  and/or  $4.6\ \mu\text{m}$ , and (in most cases) the visible magnitude are available from archival observations. Follow-up studies such as [Mainzer et al. \(2011b\)](#) and [Wright et al. \(2018\)](#) have employed NEATM and confirmed the reliability of the thermal model.

To compute physical characteristics of asteroids beyond the size and albedo, complex models called thermophysical models have been formulated by Lagerros (1996), Rozitis & Green (2011), Hanuš et al. (2015), and others. We used the Spherical, Cratered, Rotating, Energy-conserving Asteroid Model (simply called TPM in this paper) — developed by Wright (2007) and Koren et al. (2015) and validated by Masiero et al. (2019) — which models the asteroid as a rotating cratered sphere (or a triaxial ellipsoid) and uses thermal IR flux measurements to determine its diameter, albedo, and thermal inertia. Unlike STM or NEATM where surface roughness is approximated by the beaming parameter, the TPM varies the fraction of the craters on the facets, and calculates the thermal emission of all the idealized craters by accounting for the incident solar flux, blackbody radiation, solar reflection, and heat conduction. Best fits for up to ten different free parameters — the RA and Dec of the spin axis pole position, diameter, visual albedo, rotational period, thermal inertia, cratering fraction, the  $p_{\text{IR}}/p_{\text{V}}$  ratio, and the  $b/a$  and  $c/b$  axis ratios — can be computed by employing an affine-invariant Markov Chain Monte Carlo simulation (adapted from Foreman-Mackey et al. 2013).

Priors for the different parameters mentioned above are assumed. For rotational pole position, the prior is uniform in  $4\pi$ . The prior for the diameter is a log-uniform distribution of values between 1 m - 1000 km, and the same for visual albedo is a mixture model of two Rayleigh distributions given by Wright et al. (2016). The rotational period prior is modeled as a log-Cauchy distribution in terms of the equatorial rotational velocity but is heavily penalized for periods  $\leq 2$  hours if  $D \geq 200$  m (although for Apophis, the rotational period was fixed as described in the last paragraph of

this section). The prior for the cratering fraction ( $f_c$ ) is uniform in 0 - 1, and a penalty of  $-2\ln[f_c(1 - f_c)/4]$  is added to the  $\chi^2$  to make the prior uniform in  $f_c$ . The surface roughness is parametrized by the cratering fraction with a slope of  $75^\circ$  and a variable fraction of flat terrain. The prior of the thermal inertia ( $\Gamma$ ) is a log-uniform distribution for values 2.5 - 2500  $\text{Jm}^{-2}\text{s}^{-\frac{1}{2}}\text{K}^{-1}$  with a width of one unit of natural log. And finally, the prior of  $p_{\text{IR}}/p_{\text{V}}$  is  $0.563 \pm 0.340$  based on Mainzer et al. (2011a).<sup>6</sup> Cutoffs are enforced for the period and  $\Gamma$  prior by adding a penalty to the  $\chi^2$  when a model is outside the allowed range. These penalties are of the form  $[\ln(\text{parameter}/\text{limit})/\text{width}]^2$  but only applied if parameter is greater than the upper limit or if the parameter is less than the lower limit. The walkers update their position and compute a new parameter set using the equation  $p_t = p_1 + (p_2 - p_1)z$ , where  $z$  is in the range 0.5 to 2 and the square root of  $z$  is uniformly distributed, and ultimately, the goodness of fit is determined by a robust chi-square test.

For (99942) Apophis, measurements at both 3.4  $\mu\text{m}$  and 4.6  $\mu\text{m}$  bands were applied to the NEATM and TPM to derive size and visual albedo estimates. Thermal inertia ( $\Gamma$ ), crater fraction, and axis ratios were also calculated by the TPM.

For implementing NEATM, values for the beaming parameter and the ratio of infrared to visible albedos ( $p_{\text{V}}/p_{\text{IR}}$ ) were assumed based on prior measurements of these quantities from cases where more thermally-dominated infrared bands were available. Beaming was assumed to

<sup>6</sup> In the triaxial ellipsoid shape model, along with the eight parameters previously listed, uniform priors are assumed for  $(b/a)^4$  and  $(c/b)^4$  in the range 0 - 1. The distribution of  $b/a$  is supplied by the lightcurve amplitudes, and the diameter is computed as  $D = 2 * (abc)^{\frac{1}{3}}$ .

be  $1.4 \pm 0.5$  and  $p_{W1}/p_V$  was assumed to be  $1.6 \pm 1.0$  based on Mainzer et al. (2011c) and Masiero et al. (2021a); the slope parameter  $G$  was set to  $0.25 \pm 0.2$  — a value appropriate for S-type asteroids (Delbo et al. 2007 and Vereš et al. 2015) — and the H-mag was set to the derived value of  $19.1 \pm 0.5$ . For the first epoch, only the W2 band data were used as observations in W1 were too faint to produce reliable results. However, the object was much brighter during the second epoch of observations, and data from both the bands were used. NEATM analysis on the first epoch data returned a diameter of  $306 \pm 86$  m and a geometric albedo of  $0.43 \pm 0.24$ , and applying the same on the second epoch data yielded a diameter of  $406 \pm 123$  m and a visible geometric albedo of  $0.29 \pm 0.20$ . The average effective spherical diameter was calculated to be  $355 \pm 75$  m, and the average visible geometric albedo was found to be  $0.36 \pm 0.16$ . Results obtained were in agreement with systematic uncertainties associated with NEOWISE diameter and albedo estimates derived solely using  $3.4 \mu\text{m}$  and  $4.6 \mu\text{m}$  photometry (expected to be  $\sim 20\%$  and  $\sim 40\%$ , respectively, as shown by Mainzer et al. 2012 and Masiero et al. 2012). Figure 3 contains the lightcurve information from the two sets of observations.

For the TPM, the average flux was computed for each band at each observing epoch. First, the spherical shape model (also denoted as spherical TPM in this paper) was employed with a fixed rotational period of 30.568 hours,<sup>7</sup> a  $G$ -value of 0.25, an  $H$ -value of  $19.1 \pm 0.5$ , and an emissivity of 0.9. Two hundred priors were generated, and after 48,600 Markov chain loops,

<sup>7</sup> The rotational period was computed by averaging the five different results listed in Loera-González et al. (2021) along with the rotational period derived by Augustin and Behrend (2021).

the TPM yielded an effective diameter of  $340 \pm 65$  m, an effective visible geometric albedo of  $0.31 \pm 0.09$ , and thermal inertia ( $\Gamma$ ) in the range of  $350 - 3400 \text{ Jm}^{-2}\text{s}^{-\frac{1}{2}}\text{K}^{-1}$  with a best fit value of  $950 \text{ Jm}^{-2}\text{s}^{-\frac{1}{2}}\text{K}^{-1}$ . The crater fraction was found to be  $0.49^{+0.32}_{-0.31}$ . The thermophysical results were further constrained using the LCDB (Warner et al. 2019) pole solution for Apophis —  $(\alpha, \delta) = (119^\circ, -79^\circ)$  with a search radius of  $50^\circ$ . In this case, the TPM yielded an effective diameter of  $330 \pm 50$  m, an effective visible geometric albedo of  $0.32 \pm 0.08$ ,  $\Gamma \sim 300 - 2150 \text{ Jm}^{-2}\text{s}^{-\frac{1}{2}}\text{K}^{-1}$  with a best fit value of  $700 \text{ Jm}^{-2}\text{s}^{-\frac{1}{2}}\text{K}^{-1}$ , and a crater fraction equal to  $0.46^{+0.33}_{-0.28}$ .

(99942) Apophis was also modeled as a triaxial ellipsoid in the TPM (referred to as triaxial TPM in this paper) and run with the same rotational period,  $H$ ,  $G$ , and emissivity values as the spherical model. With the triaxial implementation, the TPM yielded an effective diameter of  $330 \pm 90$  m, an effective visible geometric albedo of  $0.31 \pm 0.10$ , a crater fraction of  $0.51^{+0.34}_{-0.34}$ ,  $b/a$  axis ratio equal to  $0.63^{+0.10}_{-0.12}$ ,  $c/b$  axis ratio equal to  $0.85^{+0.11}_{-0.21}$ , and thermal inertia ( $\Gamma$ ) in the range of  $100 - 2800 \text{ Jm}^{-2}\text{s}^{-\frac{1}{2}}\text{K}^{-1}$  with a best fit value of  $500 \text{ Jm}^{-2}\text{s}^{-\frac{1}{2}}\text{K}^{-1}$ . Similar to the spherical model, the triaxial TPM implementation was further constrained using the LCDB pole solution for Apophis. This yielded an effective diameter of  $340 \pm 70$  m, an effective visible geometric albedo of  $0.31 \pm 0.09$ , a crater fraction of  $0.52^{+0.34}_{-0.34}$ ,  $b/a$  axis ratio equal to  $0.63^{+0.10}_{-0.15}$ ,  $c/b$  axis ratio equal to  $0.87^{+0.10}_{-0.18}$ , and  $\Gamma \sim 150 - 2850 \text{ Jm}^{-2}\text{s}^{-\frac{1}{2}}\text{K}^{-1}$  with a best fit value of  $550 \text{ Jm}^{-2}\text{s}^{-\frac{1}{2}}\text{K}^{-1}$ . The plots in figure 4 and figure 5 are associated with the TPM, and they display the flux during the two epochs, the effective spherical diameter of the object, the best fit thermal inertia value, and the distribution of the visual albedo results.

#### 4. DISCUSSION

Delbo et al. (2007) were the first to present size and visible albedo estimations of (99942) Apophis using polarimetric observations from the 8.2 m VLT-Kueyen telescope of the European Southern Observatory, finding  $p_V = 0.33 \pm 0.08$  and  $D_{\text{eff}} = 270 \pm 60$  meters. Müller et al. (2014) used far-infrared observations from the Herschel Space Telescope PACs instrument and estimated  $D_{\text{eff}} = 375_{-10}^{+14}$  m and  $p_V = 0.3_{-0.06}^{+0.05}$ . Licandro et al. (2016) combined Herschel-PACS data with GTC/CanariCam data and reported an effective diameter between 380 - 393 meters and a visible albedo in the range 0.24 - 0.33. Brozović et al. (2018) found a best fit diameter of  $340 \pm 40$  m and a visible albedo of  $0.35 \pm 0.10$  by examining (99942) Apophis using radar observations from Goldstone and Arecibo, and rendering it as a 3D model using lightcurve-derived shape and spin states from Pravec et al. (2014). Our effective diameter and visible albedo estimate for Apophis from both NEATM and TPM are consistent with estimates put forward by Müller et al. (2014), Licandro et al. (2016), and Brozović et al. (2018) to within the measurement uncertainties.

Our results show that Apophis most likely has a thermal inertia value  $\sim 550 \text{ Jm}^{-2}\text{s}^{-\frac{1}{2}}\text{K}^{-1}$ , and such a value suggests that the asteroid's surface may consist of small and moderately-sized boulders possibly interspersed with coarse sand. Our derived thermal inertia result overlaps with estimated ranges cited in the previous studies. The same study by Müller et al. (2014) found a thermal inertia in the range of 250 - 800  $\text{Jm}^{-2}\text{s}^{-\frac{1}{2}}\text{K}^{-1}$  with a best fit at 600  $\text{Jm}^{-2}\text{s}^{-\frac{1}{2}}\text{K}^{-1}$ , and Licandro et al. (2016) cited a thermal inertia in the range of 50 - 500  $\text{Jm}^{-2}\text{s}^{-\frac{1}{2}}\text{K}^{-1}$ . A much lower value of  $\Gamma = 100_{-100}^{+240} \text{ Jm}^{-2}\text{s}^{-\frac{1}{2}}\text{K}^{-1}$  was also put forward by Yu et al. (2017). For comparison, Itokawa — an asteroid very similar

to Apophis in size and taxonomic class — was measured to have a  $\Gamma = 700 \pm 200 \text{ Jm}^{-2}\text{s}^{-\frac{1}{2}}\text{K}^{-1}$  by Müller et al. (2014). However, low thermal inertia values cannot be dismissed given the case of Bennu ( $\Gamma \sim 300 \text{ Jm}^{-2}\text{s}^{-\frac{1}{2}}\text{K}^{-1}$ ) where surface property predictions based on remote observations were incongruent with those based on in-situ observations (Rozitis et al. 2020).

The TPM may seem preferable over the NEATM since it can be used to compute parameters beyond diameter and albedo such as spin axis or thermal inertia; however, both thermal models are useful depending on the type and quantity of the data, and the goal of the study. The NEATM is highly computationally efficient, consuming seconds to minutes to produce results for a single object such as Apophis, whereas the TPM takes several hours to do the same. The NEATM is most appropriate for objects where only a single viewing geometry and a limited number of wavelengths are available. On the other hand, the TPM is suitable in cases where multi-epoch observations in a thermally-dominated wavelength are available. In the case of (99942) Apophis, both epochs of W2 observations are thermally dominated as the heliocentric distance of the object was roughly 1 au.

Regardless of the thermal model used, appropriate selection of the phase curve slope parameter  $G$  is necessary to accurately determine the apparent visible magnitude from the absolute magnitude ( $H$ ) at the time of the NEOWISE IR observations. For an S-class or an Sq-class asteroid like Apophis, the  $G$ -value is typically assumed to be 0.25. We used the average phase integral value ( $q = 0.47 \pm 0.15$ ) put forward by Shevchenko et al. (2019) to calculate a  $G = 0.25 \pm 0.20$ . Veres et al. (2015) and Colazo et al. (2021) have computed a value of  $G \sim 0.20$  for such asteroids, but this value is within the

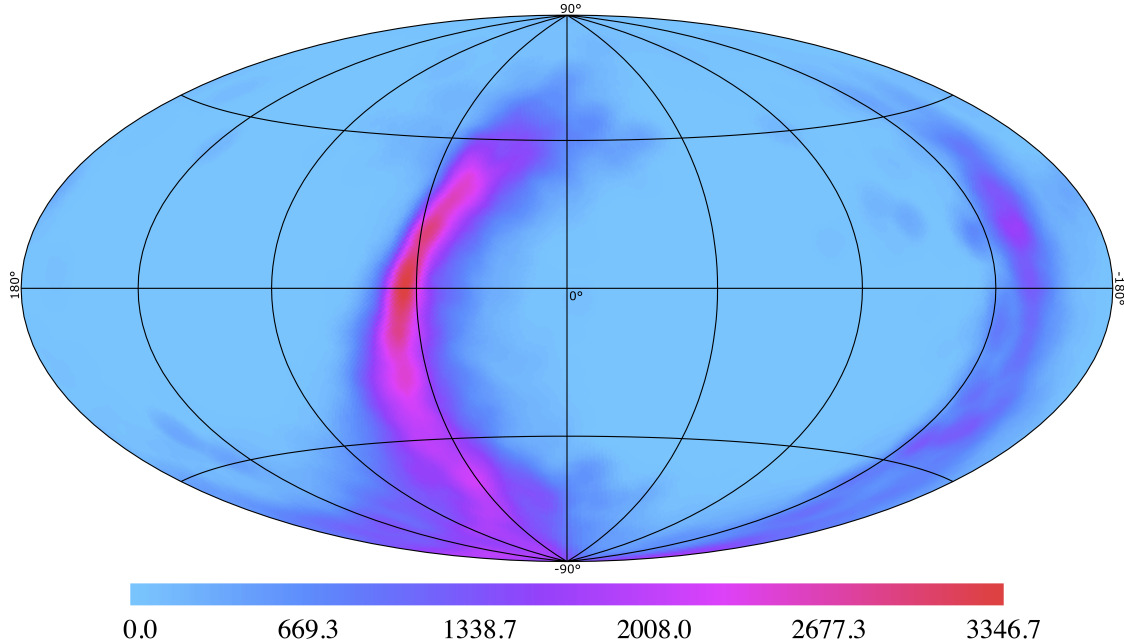


**Figure 6.** Spin pole position solution with emissivity of 0.9 as constrained by the triaxial TPM plotted in celestial coordinates. The peak pole position was found at an RA of  $50.6^\circ$  and a Dec of  $0^\circ$ . The color bar denotes the number of solutions in the bin.

measurement uncertainty range and does not seem to have a noticeable effect on the results. For instance, taking  $G = 0.2 \pm 0.1$  gives a result of  $D_{\text{eff}} = 355 \pm 79$  m and  $p_V = 0.387 \pm 0.302$  using the NEATM, and a  $D_{\text{eff}} = 365 \pm 63$  m and  $p_V = 0.33 \pm 0.10$  via the TPM; while larger variations in the slope parameter would affect the resultant visual albedo, estimates for  $G = 0.20 \pm 0.10$  and  $G = 0.25 \pm 0.10$  are virtually identical. Small changes in the absolute magnitude  $H$ , however, drastically affect V-albedo as shown by Masiero et al. (2021b). The Horizons catalog H-mag of 19.7 was, thus, not used in the thermal models because  $H$  estimates for NEAs tend to be imprecise due to poor sampling of the phase curve over a small range of phase angles. Near-simultaneous photometry from CTIO enabled us to calculate  $H = 19.1 \pm 0.5$  (for comparison, Pravec et al. 2014 reported a similar  $H$ -value of  $19.09 \pm 0.19$ ).

Considerations regarding the choice of emissivity value and pole positions were also made.

Studies show that meteorite samples and asteroid analogs typically have emissivities close to 0.9 in the low-IR and mid-IR ranges (Donaldson Hanna et al. 2019 and Maturilli et al. 2016). Rozitis et al. (2018) noted that an emissivity of 0.9 is a fair assumption at all observed wavelengths as thermophysical models have been able to reproduce 4 - 40  $\mu\text{m}$  observations of various asteroids. We quantified the influence of emissivity by running the TPM with the NEOWISE’s Apophis observations using emissivity values of 0.8, 0.9, 0.95, and 0.99. No significant differences were observed in the TPM results for the four different emissivity values (see Table 4). The mean pole positions computed in the four scenarios were also virtually identical (spin-pole results for emissivity of 0.9 can be found in Figure 6). Thus, an emissivity of 0.9 was used for the final TPM implementation.

Reflected light contributions were also considered to ensure that the bands were thermally

**Table 4.** TPM results for (99942) Apophis for four different emissivity values.

Emissivity	Diameter Meters	Albedo	Thermal inertia $\text{Jm}^{-2}\text{s}^{-\frac{1}{2}}\text{K}^{-1}$
0.80	$320 \pm 60$	$0.33 \pm 0.10$	$1050_{-700}^{+2150}$
0.90	$340 \pm 65$	$0.31 \pm 0.09$	$950_{-600}^{+2450}$
0.95	$340 \pm 70$	$0.31 \pm 0.09$	$900_{-600}^{+2750}$
0.99	$350 \pm 70$	$0.31 \pm 0.09$	$900_{-600}^{+2400}$
0.80	$320 \pm 80$	$0.31 \pm 0.10$	$400_{-350}^{+2250}$
0.90	$330 \pm 90$	$0.30 \pm 0.10$	$500_{-400}^{+2300}$
0.95	$330 \pm 80$	$0.31 \pm 0.10$	$400_{-350}^{+1850}$
0.99	$330 \pm 90$	$0.30 \pm 0.10$	$350_{-300}^{+1800}$

NOTE—The results shown are TPM implementations without the LCDB pole solution constraint. The top four rows are results from the spherical TPM, and the bottom four are from the triaxial TPM.

dominated during the observations. In our implementation of the NEATM, if more than three-quarters of the light in the first band comprises of reflected light, then fitting is redone with the infrared albedo as a free parameter (the thresholds are different if three or more detections exist). In the case of NEOWISE’s (99942) Apophis observations, the reflected light contributions were  $\sim 57\%$  in W1 and  $\sim 1\%$  in W2 in Epoch 2. The same for the latter was  $\sim 2\%$  in Epoch 1 (W1 observations from Epoch 1 were discarded during the NEATM fitting routine due to their low signal to noise ratios.). Therefore, W2 was thermally dominated during both the observing epochs, indicating that there is sufficient thermal flux for thermal modeling.

In this paper, the TPM was employed using both the LCDB pole solution and the pole solution constrained using NEOWISE’s Apophis data. The use of the LCDB pole solution is intended to demonstrate how rotational state data, which could be obtained during a close-approach event, would improve the TPM results

and greatly benefit Planetary Defense. The triaxial TPM was implemented under the assumption that if the object were to truly impact Earth, a coordinated campaign to determine the shape from light curve inversion would have been carried out. Although not part of the exercise as it was undertaken, such kind of data could have been acquired during a close-pass epoch if additional resources had been brought to bear. Further areas of improvement could include combining NEOWISE data with Herschel’s and implementing the triaxial (or a more complex) shape model in the TPM to better constrain the size, albedo, and thermal inertia. The same could be achieved through multi-epoch thermal observations as well, although such observations are hard to obtain from NEOWISE due to a fixed scanning pattern and limited mission time. Upcoming projects like the Near-Earth Object Surveyor (NEOS; Mainzer et al. 2015) could make it possible to obtain multi-epoch data in wavelengths dominated by the thermal emission of asteroids. Future studies could theorize the effect of a large thermal inertia value on the Yarkovsky drift (Bottke et al. 2002) and close-approach gravitational perturbations (Chodas 1999).

## 5. CONCLUSION

Independent measurements from NEOWISE helped estimate (99942) Apophis’ size, visual albedo, and thermal inertia during the 2020-21 planetary defense exercise. As a summary, our analyses returned the following results:

- An absolute visual magnitude of  $19.1 \pm 0.5$  using a slope parameter of  $0.25 \pm 0.20$ .
- From the NEATM, an effective spherical diameter of  $355 \pm 75$  m and an average geometric albedo of  $0.36 \pm 0.16$ .
- From the spherical TPM with the LCDB pole solution, an effective diameter of 330

**Table 5.** Table summarizing the thermophysical results for (99942) Apophis.

Diameter	Albedo	Thermal inertia	Reference
Meters		$\text{Jm}^{-2}\text{s}^{-\frac{1}{2}}\text{K}^{-1}$	
$270 \pm 60$	$0.33 \pm 0.08$	-	Delbo et al. (2007)
$375_{-10}^{+14}$	$0.30_{-0.06}^{+0.05}$	-	Müeller et al. (2014)
380 - 393	0.24 - 0.33	50 - 500	Licandro et al. (2016)
$340 \pm 40$	$0.35 \pm 0.10$	600	Brozović et al. (2018)
$340 \pm 70$	$0.31 \pm 0.09$	550	This Paper

$\pm 50$  m, an effective geometric albedo of  $0.32 \pm 0.08$ , and a  $\Gamma = 700_{-400}^{+1450}$   $\text{Jm}^{-2}\text{s}^{-\frac{1}{2}}\text{K}^{-1}$ .

- From the triaxial TPM with the LCDB pole solution, an effective diameter of  $340 \pm 70$  m, an effective geometric albedo of  $0.31 \pm 0.09$ , and a  $\Gamma = 550_{-400}^{+2300}$   $\text{Jm}^{-2}\text{s}^{-\frac{1}{2}}\text{K}^{-1}$ .

The estimated diameter derived from the “discovery” observations allowed exercise participants to calculate that the object would produce  $\sim 8.5 \times 10^{19}$  J (or  $2 \times 10^7$  kilotons of TNT) of energy upon impact.<sup>8</sup> Although this estimate is a factor of  $10^4$  larger than the estimated energy produced by Chelyabinsk, the participants quickly determined that the object would most likely cause a regional disaster and not a global one.

Thus, we demonstrate that the NEOWISE data and thermal modeling are capable of rapid and accurate physical characterization of Near-Earth Asteroids (NEAs), and highlight that such expeditious data processing could prove to be essential in assessing threat levels and

mitigating hazards posed by them.

## 6. ACKNOWLEDGEMENTS

The NEOWISE Reactivation Mission is funded by the NASA Science Mission Directorate Planetary Science Division as part of the Planetary Defense Coordination Office. Dr. Amy Mainzer of the University of Arizona is the NEOWISE Principal Investigator. NEOWISE is managed and operated by JPL. Data processing, archiving and distribution for NEOWISE is carried out by IPAC, California Institute of Technology. Operations of the NEOWISE spacecraft and payload are supported by Ball Aerospace and Technology Corp. and the Space Dynamics Laboratory, Utah State University.

NEOWISE gratefully acknowledges the services contributed by the IAU Minor Planet Center, operated by the Harvard-Smithsonian Center for Astrophysics.

NEOWISE makes use of data from the WISE, AllWISE, and original NEOWISE projects that were funded by the NASA Astrophysics and Planetary Science Divisions.

The work of EK and JP was conducted at the Jet Propulsion laboratory, California Institute of Technology, under a contract with the Na-

<sup>8</sup> Density was assumed to be  $2700 \text{ kgm}^{-3}$  from Carry (2012), and impact velocity was assumed to be  $20 \text{ kms}^{-1}$  from Harris & Hughes (1994) and French (1998).



tional Aeronautics and Space Administration (80NM0018D0004).

We are also thankful for the High Performance Computing (HPC) resources provided by the University of Arizona TRIF, UITS, and

Research, Innovation, and Impact (RII) and maintained by the UArizona Research Technologies department.

*Software:* astropy (Astropy Collaboration et al. 2013, 2018), scipy (Virtanen et al. 2020), numpy (Harris et al. 2020)

## REFERENCES

- Astropy Collaboration, Robitaille, T. P., Tollerud, E. J., et al. 2013, *A&A*, 558, A33, doi: [10.1051/0004-6361/201322068](https://doi.org/10.1051/0004-6361/201322068)
- Astropy Collaboration, Price-Whelan, A. M., Sipócz, B. M., et al. 2018, *AJ*, 156, 123, doi: [10.3847/1538-3881/aabc4f](https://doi.org/10.3847/1538-3881/aabc4f)
- Binzel, R. P., Xu, S., Bus, S. J., & Howell, E. 1992, *Science*, 257, 779, doi: [10.1126/science.257.5071.779](https://doi.org/10.1126/science.257.5071.779)
- Binzel, R. P., Rivkin, A. S., Thomas, C. A., et al. 2009, *Icarus*, 200, 480, doi: [10.1016/j.icarus.2008.11.028](https://doi.org/10.1016/j.icarus.2008.11.028)
- Borovička, J., Spurný, P., Brown, P., et al. 2013, *Nature*, 503, 235, doi: [10.1038/nature12671](https://doi.org/10.1038/nature12671)
- Bottke, W. F., J., Vokrouhlický, D., Rubincam, D. P., & Broz, M. 2002, The Effect of Yarkovsky Thermal Forces on the Dynamical Evolution of Asteroids and Meteoroids, 395–408
- Bowell, E., Hapke, B., Domingue, D., et al. 1989, in *Asteroids II*, ed. R. P. Binzel, T. Gehrels, & M. S. Matthews, 524–556
- Brozovic, M., Benner, L., McMichael, J., et al. 2018, *Icarus*, 300, 115
- Bus, S. J. 1999, PhD thesis, MASSACHUSETTS INSTITUTE OF TECHNOLOGY
- Carry, B. 2012, *Planet. Space Sci.*, 73, 98, doi: [10.1016/j.pss.2012.03.009](https://doi.org/10.1016/j.pss.2012.03.009)
- Chodas, P. W. 1999, in *Bulletin of the American Astronomical Society*, Vol. 31, 1117
- Colazo, M., Duffard, R., & Weidmann, W. 2021, *Monthly Notices of the Royal Astronomical Society*, 504, 761–768, doi: [10.1093/mnras/stab726](https://doi.org/10.1093/mnras/stab726)
- Cutri, R. M., Wright, E. L., Conrow, T., et al. 2013, Explanatory Supplement to the AllWISE Data Release Products, Explanatory Supplement to the AllWISE Data Release Products
- Cutri, R. M., Mainzer, A., Conrow, T., et al. 2015, Explanatory Supplement to the NEOWISE Data Release Products, Explanatory Supplement to the NEOWISE Data Release Products
- Delbo, M., Cellino, A., & Tedesco, E. 2007, *Icarus*, 188, 266, doi: [10.1016/j.icarus.2006.12.024](https://doi.org/10.1016/j.icarus.2006.12.024)
- DeMeo, F. E., Binzel, R. P., Slivan, S. M., & Bus, S. J. 2009, *Icarus*, 202, 160, doi: [10.1016/j.icarus.2009.02.005](https://doi.org/10.1016/j.icarus.2009.02.005)
- Donaldson Hanna, K. L., Schrader, D. L., Cloutis, E. A., et al. 2019, *Icarus*, 319, 701, doi: [10.1016/j.icarus.2018.10.018](https://doi.org/10.1016/j.icarus.2018.10.018)
- Foreman-Mackey, D., Hogg, D. W., Lang, D., & Goodman, J. 2013, *PASP*, 125, 306, doi: [10.1086/670067](https://doi.org/10.1086/670067)
- French, B. M. 1998, *Traces of Catastrophe: A Handbook of Shock-Metamorphic Effects in Terrestrial Meteorite Impact Structures*
- Granvik, M., & Brown, P. 2018, *Icarus*, 311, 271, doi: [https://doi.org/10.1016/j.icarus.2018.04.012](https://doi.org/https://doi.org/10.1016/j.icarus.2018.04.012)
- Hanuš, J., Delbo, M., Ďurech, J., & Alí-Lagoa, V. 2015, *Icarus*, 256, 101, doi: [10.1016/j.icarus.2015.04.014](https://doi.org/10.1016/j.icarus.2015.04.014)
- Harris, A. W. 1998, *Icarus*, 131, 291, doi: [10.1006/icar.1997.5865](https://doi.org/10.1006/icar.1997.5865)
- Harris, A. W., & Lagerros, J. S. V. 2002, *Asteroids in the Thermal Infrared*, 205–218
- Harris, C. R., Millman, K. J., van der Walt, S. J., et al. 2020, *Nature*, 585, 357–362, doi: [10.1038/s41586-020-2649-2](https://doi.org/10.1038/s41586-020-2649-2)
- Harris, N. W., & Hughes, D. W. 1994, *Planet. Space Sci.*, 42, 285, doi: [10.1016/0032-0633\(94\)90098-1](https://doi.org/10.1016/0032-0633(94)90098-1)
- Jones, T. J., & Morrison, D. 1974, *AJ*, 79, 892, doi: [10.1086/111626](https://doi.org/10.1086/111626)

- Koren, S. C., Wright, E. L., & Mainzer, A. 2015, *Icarus*, 258, 82, doi: [10.1016/j.icarus.2015.06.014](https://doi.org/10.1016/j.icarus.2015.06.014)
- Kostov, A., & Bonev, T. 2018, *Bulgarian Astronomical Journal*, 28, 3, <https://arxiv.org/abs/1706.06147>
- Lagerros, J. S. V. 1996, *A&A*, 310, 1011
- Lauretta, D. S., Balram-Knutson, S. S., Beshore, E., et al. 2017, *SSRv*, 212, 925, doi: [10.1007/s11214-017-0405-1](https://doi.org/10.1007/s11214-017-0405-1)
- Lebofsky, L. A., & Spencer, J. R. 1989, in *Asteroids II*, ed. R. P. Binzel, T. Gehrels, & M. S. Matthews, 128–147
- Lebofsky, L. A., Sykes, M. V., Tedesco, E. F., et al. 1986, *Icarus*, 68, 239, doi: [https://doi.org/10.1016/0019-1035\(86\)90021-7](https://doi.org/10.1016/0019-1035(86)90021-7)
- Licandro, J., Müller, T., Alvarez, C., Alí-Lagoa, V., & Delbo, M. 2016, *A&A*, 585, A10, doi: [10.1051/0004-6361/201526888](https://doi.org/10.1051/0004-6361/201526888)
- Lin, C.-H., Ip, W.-H., Lin, Z.-Y., et al. 2018, *Planet. Space Sci.*, 152, 116, doi: [10.1016/j.pss.2017.12.019](https://doi.org/10.1016/j.pss.2017.12.019)
- Loera-González, P., Olguín, L., Saucedo-Morales, J., Núñez-López, R., & Domínguez-González, R. 2021, *Minor Planet Bulletin*, 48, 203
- Mainzer, A., Bauer, J., Grav, T., et al. 2011a, *ApJ*, 731, 53, doi: [10.1088/0004-637X/731/1/53](https://doi.org/10.1088/0004-637X/731/1/53)
- Mainzer, A., Grav, T., Masiero, J., et al. 2011b, *ApJ*, 736, 100, doi: [10.1088/0004-637X/736/2/100](https://doi.org/10.1088/0004-637X/736/2/100)
- . 2011c, *ApJ*, 741, 90, doi: [10.1088/0004-637X/741/2/90](https://doi.org/10.1088/0004-637X/741/2/90)
- . 2012, *ApJL*, 760, L12, doi: [10.1088/2041-8205/760/1/L12](https://doi.org/10.1088/2041-8205/760/1/L12)
- Mainzer, A., Bauer, J., Cutri, R. M., et al. 2014, *ApJ*, 792, 30, doi: [10.1088/0004-637X/792/1/30](https://doi.org/10.1088/0004-637X/792/1/30)
- Mainzer, A., Grav, T., Bauer, J., et al. 2015, *AJ*, 149, 172, doi: [10.1088/0004-6256/149/5/172](https://doi.org/10.1088/0004-6256/149/5/172)
- Masiero, J. R., Mainzer, A. K., Bauer, J. M., et al. 2021a, *PSJ*, 2, 162, doi: [10.3847/PSJ/ac15fb](https://doi.org/10.3847/PSJ/ac15fb)
- Masiero, J. R., Mainzer, A. K., Grav, T., et al. 2012, *ApJL*, 759, L8, doi: [10.1088/2041-8205/759/1/L8](https://doi.org/10.1088/2041-8205/759/1/L8)
- Masiero, J. R., Wright, E. L., & Mainzer, A. K. 2019, *AJ*, 158, 97, doi: [10.3847/1538-3881/ab31a6](https://doi.org/10.3847/1538-3881/ab31a6)
- . 2021b, *PSJ*, 2, 32, doi: [10.3847/PSJ/abda4d](https://doi.org/10.3847/PSJ/abda4d)
- Matson, D. L. 1972, PhD thesis, California Institute of Technology, doi: [10.7907/Y25B-JY16](https://doi.org/10.7907/Y25B-JY16)
- Maturilli, A., Helbert, J., Ferrari, S., Davidsson, B., & D'Amore, M. 2016, *Earth, Planets and Space*, 68, 113, doi: [10.1186/s40623-016-0489-y](https://doi.org/10.1186/s40623-016-0489-y)
- Michel, P., Morbidelli, A., & Bottke, W. F. 2005, *Comptes Rendus Physique*, 6, 291, doi: <https://doi.org/10.1016/j.crhy.2004.12.013>
- Morrison, D. 1973, *Icarus*, 19, 1, doi: [10.1016/0019-1035\(73\)90134-6](https://doi.org/10.1016/0019-1035(73)90134-6)
- Morrison, D., & Chapman, C. R. 1976, *ApJ*, 204, 934, doi: [10.1086/154242](https://doi.org/10.1086/154242)
- Morrison, D., & Lebofsky, L. 1979, *Radiometry of asteroids.*, ed. T. Gehrels & M. S. Matthews, 184–205
- Mueller, T., Kiss, C., Scheirich, P., et al. 2014, *Astronomy & Astrophysics*, 566, doi: [10.1051/0004-6361/201423841](https://doi.org/10.1051/0004-6361/201423841)
- Müller, T. G., Hasegawa, S., & Usui, F. 2014, *PASJ*, 66, 52, doi: [10.1093/pasj/psu034](https://doi.org/10.1093/pasj/psu034)
- Ostro, S. J. 1993, *Rev. Mod. Phys.*, 65, 1235, doi: [10.1103/RevModPhys.65.1235](https://doi.org/10.1103/RevModPhys.65.1235)
- Pravec, P., Scheirich, P., Durech, J., et al. 2014, *Icarus*, 233, 48, doi: <https://doi.org/10.1016/j.icarus.2014.01.026>
- Reddy, V., Kelley, M. S., Farnocchia, D., et al. 2019, *Icarus*, 326, 133, doi: [10.1016/j.icarus.2019.02.018](https://doi.org/10.1016/j.icarus.2019.02.018)
- Rozitis, B., & Green, S. F. 2011, *MNRAS*, 415, 2042, doi: [10.1111/j.1365-2966.2011.18718.x](https://doi.org/10.1111/j.1365-2966.2011.18718.x)
- Rozitis, B., Green, S. F., MacLennan, E., & Emery, J. P. 2018, *MNRAS*, 477, 1782, doi: [10.1093/mnras/sty640](https://doi.org/10.1093/mnras/sty640)
- Rozitis, B., Ryan, A. J., Emery, J. P., et al. 2020, *Science Advances*, 6, doi: [10.1126/sciadv.abc3699](https://doi.org/10.1126/sciadv.abc3699)
- Shevchenko, V. G., Belskaya, I. N., Mikhalechenko, O. I., et al. 2019, *A&A*, 626, A87, doi: [10.1051/0004-6361/201935588](https://doi.org/10.1051/0004-6361/201935588)
- Tholen, D. J. 1984, PhD thesis, University of Arizona, Tucson
- Vasilyev, N. V. 1998, *Planet. Space Sci.*, 46, 129, doi: [10.1016/S0032-0633\(97\)00145-1](https://doi.org/10.1016/S0032-0633(97)00145-1)
- Veeder, G. J., Hanner, M. S., Matson, D. L., et al. 1989, *AJ*, 97, 1211, doi: [10.1086/115064](https://doi.org/10.1086/115064)
- Vereš, P., Jedicke, R., Fitzsimmons, A., et al. 2015, *Icarus*, 261, 34, doi: [10.1016/j.icarus.2015.08.007](https://doi.org/10.1016/j.icarus.2015.08.007)
- Virtanen, P., Gommers, R., Oliphant, T. E., et al. 2020, *Nature Methods*, 17, 261, doi: [10.1038/s41592-019-0686-2](https://doi.org/10.1038/s41592-019-0686-2)

- Warner, B. D., Harris, A. W., & Pravec, P. 2019, Asteroid Lightcurve Database (LCDB) Bundle V3.0, urn:nasa:pds:ast-lightcurve-database::3.0, NASA Planetary Data System, doi: [10.26033/7h40-8s80](https://doi.org/10.26033/7h40-8s80)
- Watanabe, S.-i., Tsuda, Y., Yoshikawa, M., et al. 2017, *SSRv*, 208, 3, doi: [10.1007/s11214-017-0377-1](https://doi.org/10.1007/s11214-017-0377-1)
- Werner, M. W., Roellig, T. L., Low, F. J., et al. 2004, *ApJS*, 154, 1, doi: [10.1086/422992](https://doi.org/10.1086/422992)
- Wright, E., Mainzer, A., Masiero, J., et al. 2018, arXiv e-prints, arXiv:1811.01454, <https://arxiv.org/abs/1811.01454>
- Wright, E. L. 2007, arXiv e-prints, astro, <https://arxiv.org/abs/astro-ph/0703085>
- Wright, E. L., Mainzer, A., Masiero, J., Grav, T., & Bauer, J. 2016, *AJ*, 152, 79, doi: [10.3847/0004-6256/152/4/79](https://doi.org/10.3847/0004-6256/152/4/79)
- Wright, E. L., Eisenhardt, P. R. M., Mainzer, A. K., et al. 2010, *AJ*, 140, 1868, doi: [10.1088/0004-6256/140/6/1868](https://doi.org/10.1088/0004-6256/140/6/1868)
- Yu, L.-L., Ji, J., & Ip, W.-H. 2017, *Research in Astronomy and Astrophysics*, 17, 070, doi: [10.1088/1674-4527/17/7/70](https://doi.org/10.1088/1674-4527/17/7/70)